Biophysical Journal
Article

Biophysical Society

The Kinetics of Nucleotide Binding to Isolated *Chlamydomonas* Axonemes Using UV-TIRF Microscopy

Maria Feofilova,[1] Mohammed Mahamdeh,[1] and Jonathon Howard[1,*]
[1]Yale University, New Haven, Connecticut

ABSTRACT Cilia and flagella are long, slender organelles found in many eukaryotic cells, where they have sensory, developmental, and motile functions. All cilia and flagella contain a microtubule-based structure called the axoneme. In motile cilia and flagella, which drive cell locomotion and fluid transport, the axoneme contains, along most of its length, motor proteins from the axonemal dynein family. These motor proteins drive motility by using energy derived from the hydrolysis of ATP to generate a bending wave, which travels down the axoneme. As a first step toward visualizing the ATPase activity of the axonemal dyneins during bending, we have investigated the kinetics of nucleotide binding to axonemes. Using a specially built ultraviolet total internal reflection fluorescence microscope, we found that the fluorescent ATP analog methylanthraniloyl ATP (mantATP), which has been shown to support axonemal motility, binds all along isolated, immobilized axonemes. By studying the recovery of fluorescence after photobleaching, we found that there are three mantATP binding sites: one that bleaches rapidly (time constant $\approx$ 1.7 s) and recovers slowly (time constant $\approx$ 44 s), one that bleaches with the same time constant but does not recover, and one that does not bleach. By reducing the dynein content in the axoneme using mutants and salt extraction, we provide evidence that the slow-recovering component, but not the other components, corresponds to axonemal dyneins. The recovery rate of this component, however, is too slow to be consistent with the activation of beating observed at higher mantATP concentrations; this indicates that the dyneins may be inhibited due to their immobilization at the surface. The development of this method is a first step toward direct observation of the traveling wave of dynein activity.

SIGNIFICANCE In 1958, it was hypothesized by Kenneth Machin that the movement of eukaryotic cilia and flagella is driven by a traveling wave of motor activity. However, such a wave of motor activity has never been observed because of difficulties in assaying dynein activity. We have developed an ultraviolet total internal reflection fluorescence microscope that allows us to measure the fluorescent nucleotide methylanthraniloyl ATP binding to isolated, demembranated cilia. Using mutants and salt extraction, we show that a fraction of the binding correlates with the dynein content, and using fluorescence recovery after photobleaching, we measure the kinetics of fluorescent nucleotide exchange from the dyneins. We argue that this is an important first step toward observing the traveling wave.

INTRODUCTION

Motile eukaryotic cilia and flagella are dynamic structures that move in a periodic wave-like pattern to propel cells through liquid and to move fluid across cell surfaces (1). At the core of cilia and flagella is the axoneme, a bundle of nine doublet microtubules surrounding a core of two single microtubules, together with hundreds of other associated proteins (2,3). Among these associated proteins are the axonemal dyneins, which are located between the doublets along the length of the axoneme (4). The dyneins use energy derived from the hydrolysis of ATP to slide microtubule doublets (5–7), and the sliding is converted to bending by constraints that prevent sliding at the base. The dyneins undergo an ATPase cycle: ATP binds and is hydrolyzed, and the products (ADP and organic phosphate) are released (8,9). The ATPase cycle is thought to be coupled to force

Submitted February 11, 2019, and accepted for publication July 1, 2019.

*Correspondence: jonathon.howard@yale.edu

Maria Feofilova's present address is ETH Zürich, Laboratory for Soft and Living Materials, Vladimir-Prelog-Weg 1-5/10, 8093 Zürich, Switzerland.

Mohammed Mahamdeh's present address is Cardiovascular Research Center, Massachusetts General Hospital, 149 13th Street, Charlestown, Massachusetts.

Editor: Kazuhiro Oiwa.

https://doi.org/10.1016/j.bpj.2019.07.004

generation through conformational changes of the dyneins (10–12). The similarity of the frequency of the axonemal bending wave to the ATPase rate of the axonemal dyneins suggests that each dynein ATP cycle is coupled to a cycle of doublet sliding and bending (13). In this way, dynein is thought to power the axonemal beat.

Dyneins are believed to generate sliding forces all along the length of the axoneme. First, the dyneins are present all along the length (14). And second, early modeling studies, which predated the discovery of dynein, argued that the bending wave was caused by a wave of activity that traveled all along the length: if motors were only active at the base, driving a whip-like motion of the axoneme, then the amplitude of the bending wave would decrease as it propagates (15), in contradiction to observations. The hypothesis that the axonemal bending wave is driven by a traveling wave of dynein activation forms the basis for many subsequent models, which can accurately predict the axonemal waveform (15–19). However, this hypothesized wave of dynein activity has never been directly measured or observed. Direct observation of a traveling wave of dynein activation is important not just to test the models but also to provide information about the extent of the modulation of the dynein activity, as well as its spatial and temporal properties.

One reason why it is difficult to observe directly the postulated traveling wave of dynein activation is that it is difficult to assay the activity of dynein. One experimental avenue is electron cryomicroscopy. A limitation of this approach, however, is that it is difficult to rapidly freeze a beating cilium or axoneme. For example, in a recent study (12), an active axoneme was rapidly frozen, but during the sample preparation, which took a few seconds, it is possible that beating stopped or was altered. Another avenue is to use fluorescence to monitor the binding and unbinding of ATP. However, this approach is difficult because dyneins have a higher specificity for nucleotides than other motors such as myosins and kinesins: only a small number of ATP analogs have been shown to support force generation by axonemal dyneins (20–22). Indeed, only the fluorescently labeled nucleotides 2′-(or 3′)-O-(N-methylanthraniloyl) ATP (mantATP) and 2′- (or 3′)-O-anthraniloyl ATP can support reactivation of isolated, demembranated axonemes, although at frequencies significantly reduced from that of ATP (21,23). MantATP also supports translocation of microtubules in gliding assays, in which outer-arm dyneins (24; https://www.qucosa.de/api/qucosa%3A34182/attachment/ATT-0/) or inner-arm dyneins (25) are bound to the glass surface of a perfusion chamber and microtubules introduced into the solution are observed to glide along the surface. Although the fluorescence of mantATP has been used in solution studies on axonemal dyneins (26), mantATP fluorescence has not been observed in the intact axoneme structure. This is partly due to the low quantum efficiency of the dye and partly due to the excitation and emission spectra of mantATP, which have peaks at 355 and 448 nm, respectively (https://www.jenabioscience.com/images/PDF/NU-202.0001.pdf), and make detection difficult because of the high background signal.

Recent developments in highly sensitive cameras for use with microscopy allow imaging of low-emitting dyes such as mantATP. Here, we report for the first time, to our knowledge, the direct observation of binding of mantATP to intact immobilized axonemes using ultraviolet (UV) total internal reflection fluorescence (TIRF) microscopy.

METHODS

Reagents

MantATP (trisodium salt) was purchased from Jena Bioscience (Jena, Germany). All other reagents were purchased from Sigma Aldrich (St. Louis, MO) unless stated otherwise.

Chlamydomonas cells

Chlamydomonas reinhardtii cells (CC-125 wild-type mt+ 137c) were grown in liquid tris-acetate-phosphate medium: 20 mM tris, 7 mM NH_4Cl, 0.40 mM $MgSO_4$, 0.34 mM $CaCl_2$, 2.5 mM PO^{-3}_4, and 1000-fold diluted Hutner's trace elements (14). The medium was titrated to pH 7.0 with glacial acetic acid.

Axonemes

Axonemes were purified using the method described in Alper et al. (27). *Chlamydomonas* cells were harvested by centrifugation at 900 × *g* for 5 min. They were then deflagellated by incubation with 4.2 mM dibucaine-HCl for 90 s. The flagella were separated from the cell bodies by centrifugation at 24,000 × *g* for 20 min on a 30% sucrose cushion. Flagella were then concentrated by resuspending the pellet in 10 mL of HMDE buffer (30 mM HEPES, 5 mM $MgSO_4$, 1 mM dithiothreitol, and 1 mM EGTA, titrated to pH 7.4 with KOH) with addition of 0.4 mM Pefabloc. The flagella were then demembranated by adding 0.2% IGEPAL CA-630 and washed in HMDE buffer. Salt extraction of axonemes was performed by incubating with the indicated amount of KCl (0.3–1 M) + HMDE for 20 min; the extracted axonemes were then centrifuged at 31,000 × *g* for 20 min to remove the salt and extracted protein. The axonemes were re-suspended in HMDE buffer.

Measurement of dynein content

Serial dilutions of each kind of axoneme were loaded on sodium dodecyl sulfate–polyacrylamide gel electrophoresis (SDS-PAGE) gels, 4–15% precast Mini-PROTEAN TGX gels, tris/tricine/SDS running buffer, and SDS sample buffer (BioRad, Hercules, CA). Gels were then stained with Coomassie brilliant blue (Life Technologies, Carlsbad, CA). Images of gels were obtained by scanning the gel on an Epson V700 document scanner (Epson, Suwa, Nagano, Japan). The gels were analyzed in Fiji image analysis software (16). The amount of dynein and tubulin was measured by integrating the density of the respective bands in the scanned gels. The dynein content was defined as the dynein signal divided by the tubulin signal, the latter serving as a loading control.

Imaging

Imaging was performed using a Zeiss Axiovert 200M (Zeiss, Oberkochen, Germany) microscope with a Zeiss Alpha Plan-Fluar 100×/1.45 oil

objective and a home-built laser-TIRF line (Fig. 1, Table 1). A UV diode-pumped laser (model Zouk 05-01, 355 nm, maximal power 10 mW (Cobolt, Solna, Sweden)) was used as the light source. Images were recorded with an iXon 887 electron-multiplying CCD back-illuminated camera (Andor, Belfast, UK).

For imaging, axonemes in HMDEKP buffer (30 mM HEPES, 5 mM $MgSO_4$, 1 mM dithiothreitol, and 1 mM EGTA, 50 mM K-acetate, 1% w/v polyethylene glycol, titrated to pH 7.4 with KOH) were infused into an experimental chamber of depth 0.1 mm formed by a coverslip and a microscope slide; the glass surfaces we easy-cleaned (28).

During the bleaching phase, the field of view was continuously exposed to light for 12 s. During the recovering phase, the field of view was illuminated by brief flashes of the same intensity and of 100 ms duration; the intervals between flashes varied between 5 and 25 s.

Image analysis

Collected image sequences were analyzed in MATLAB (The MathWorks, Natick, MA) with a semiautomated procedure. Line profiles were drawn along the axonemes, and the lines were widened by performing a dilation operation with a 5-pixel square structuring element to produce an axonemal region of interest. The pixels in the original image in this region were then averaged to obtain the axonemal signal (F_{axoneme}). Equivalent regions on both side of the axonemes were used to calculate a background signal ($F_{\text{background}}$). Because the background illumination varied across the field of view because of variation in the laser intensity, we normalized the axoneme signal by first subtracting the background and then dividing by the background signal to obtain a relative axoneme fluorescence intensity

$$F = \frac{F_{axoneme}}{F_{background}} - 1 \tag{1}$$

Fitting the bleaching and recovery phases

The data were analyzed separately for the bleaching phase $0 < t < t_{\text{off}}$, where the field of view is constantly exposed to the laser light, and the recovery phase $t > t_{\text{off}}$, where $t_{\text{off}} = 12$ s is the time at which the continuous laser light is shuttered (Fig. 2 *B*). The bleaching phase was fitted with the empirical equation

$$F_{bleaching}(t) = F_i - (F_i - F_0)e^{-k_1 t}, \tag{2}$$

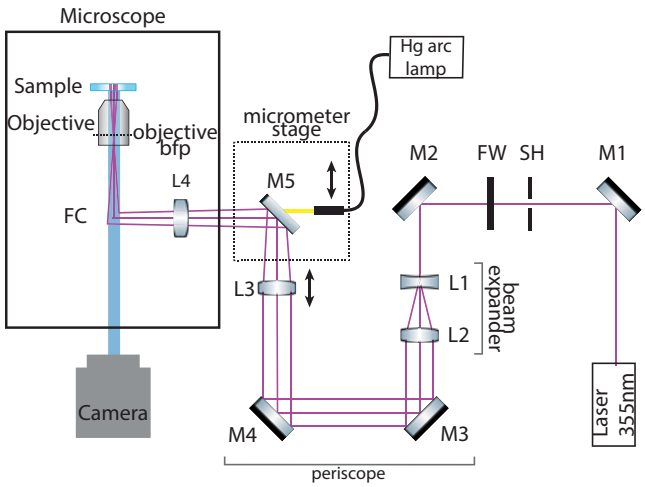

FIGURE 1 Optical schematic of the UV-TIRF; legend can be found in Table 1. To see this figure in color, go online.

and the recovery phase was fitted with

$$F_{\text{recovery}}(t) = F_r + (F_i - F_r)e^{-k_2 t} \tag{3}$$

F_0 is the initial relative fluorescence intensity value (at $t = 0$), F_i is the bleaching steady-state intensity, and F_r is the maximal recovery intensity. k_1 and k_2 are the rate constants of the bleaching and recovery phases, respectively. Separation into these two phases was possible because there was a large difference between the rate constants of the bleaching and recovery phases and because bleaching had nearly reached a steady state at t_{off}. The parameters were obtained by fitting the data to these exponential functions using nonlinear least squares (MATLAB, "fit" function).

RESULTS

MantATP binds to the axoneme

We incubated flow cells with solutions containing isolated, demembranated *Chlamydomonas* axonemes and waited a few minutes until several had bound to the surface in each field of view (82 × 82 μm). We then infused a solution containing 1 μM mantATP. Using a TIRF microscope with long-wavelength UV illumination (Fig. 1, 355 nm laser), we observed a fluorescent signal along the entire axoneme (Fig. 2 *A*, *TIRF image* in *upper panel*, *differential interference contrast image* in *lower panel*). The same assay

TABLE 1 List of Parts for the UV-TIRF Microscope Schematic

Abbreviation	Component Description	Manufacturer
Microscope	Zeiss Axiovert 200M	Zeiss
Laser	UV diode-pumped laser, model Zouk 05-01, 355 nm, maximal power 10 mW	Cobolt
Hg arc lamp	Mercury arc lamp HBO 100	Zeiss
Electronic controller	Ludl Electronic Products MAC 2002 Controller	LEP
Computer	Dell Precision T1700 workstation	Dell
M1–M4	25.4 mm mirror, UV-enhanced aluminum	ThorLabs
M5	Dichroic mirror, cutoff 400 nm long pass	Chroma
L1	Fused silica plano-concave lens F = −12.0, UV-coated	ThorLabs
L2	Fused silica plano-convex lens F = 100, UV-coated	ThorLabs
L3	Fused silica plano-convex lens F = 150, UV-coated	ThorLabs
Filter wheel	Six-position motorized filter wheel, for 25.4 mm optics FW102C	ThorLabs
Shutter	25 mm optical shutter VS25	Uniblitz
Microscope	Axiovert 200M microscope with differential interference contrast/ phase capable condenser	Zeiss
Objective	Alpha Plan-Fluar 100× NA = 1.45 oil objective	Zeiss
Camera	iXon 887 electron-multiplying CCD back-illuminated camera	Andor
Filter cube	Interchangeable filter cube (in the microscope turret). For 355 nm laser TIRF: excitation filter 355/10 nm; emission filter 460/50 nm; mirror 400 nm long pass.	Zeiss/Chroma

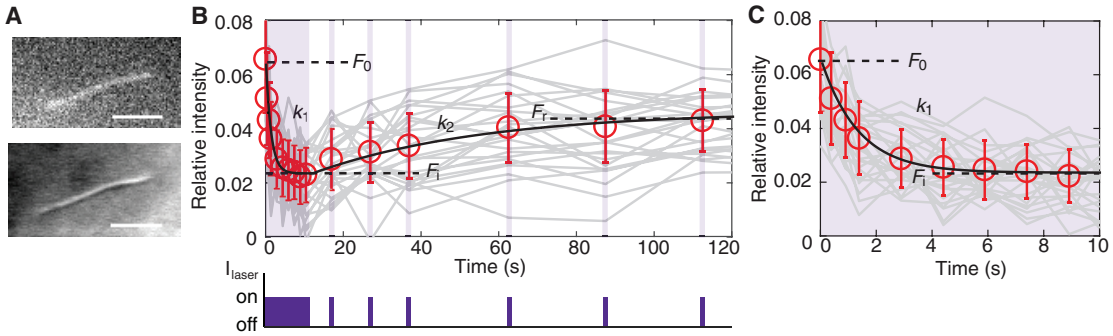

FIGURE 2 Bleaching and recovery of *oda1* axonemes under UV-TIRF. (*A*) First frame is an image of an axoneme from the experiment (*top*). A differential interference contrast image of the same axoneme is given (*bottom*). Scale bars, 5 μm. (*B*) Upper panel shows a bleaching and recovery time: mean ± SD with red circles and error bars, a random sampling of raw traces is shown in gray. Lower panel indicates the illumination sequence: 12 s constant illumination (bleaching phase) is followed by 100-ms-duration flashes of the same intensity. Fit to the data is shown with a solid black curve (see Methods). (*C*) A higher-temporal-resolution plot of the bleaching phase is shown. To see this figure in color, go online.

performed in the absence of mantATP did not produce a fluorescent signal from the axonemes. Thus, there are mantATP binding sites all the along the axoneme, though we cannot exclude the possibility that the fluorescence is reduced within a micrometer from the ends.

To investigate the kinetics of the binding and unbinding of mantATP to the axoneme, we used a bleaching and recovery protocol. In this assay, the fluorescence was bleached by intense, continuous UV illumination, and the recovery of fluorescence was monitored by intermittent brief light pulses. A typical trace is shown in Fig. 2 *B*, in which there is partial bleaching followed by partial recovery of fluorescence. During the bleaching phase, the fluorescent signal decreased over a few seconds from its initial value F_0 toward a steady-state value F_i. During the recovery phase, the fluorescent signal approached the recovery value F_r over approximately 1 min. See Table 2 for the bleaching and recovery rates, together with the amplitudes F_0, F_i, and F_r. We identified two general features of the bleaching and recovery curves: 1) the bleaching rate was much higher than the recovery rate, and 2) the recovery was always incomplete ($F_r < F_0$).

The bleaching recovery data indicate that there are at least three nucleotide-binding sites

To understand the bleaching and recovery curves, we first attempted to fit the time courses with the one-binding-site model shown in Fig. 3. The idea is that mantATP* binds to a site and is hydrolyzed to mantADP*, and the mantADP* unbinds at a slow rate. The (*) refers to the fluorescent nucleotide. If hydrolysis (h) is faster than bleaching (b)—justified by data on the ATPase activity of *Tetrahymena* outer-arm dynein (29)—then the bleaching phase corresponds to bleaching of mantADP* to mantADP†, where (†) denotes the bleached nucleotide. In this scheme, recovery is limited by the slow unbinding of mantADP†. Usually, we will omit the (†).

This one-binding-site model cannot account for the bleaching and recovery curves shown in Fig. 2 (see Appendix for the mathematical arguments). First, there should be complete recovery. Instead, the partial recovery indicates that there is a site that bleaches irreversibly. We call this the nonrecovering component. Second, the slow-recovering component should exhibit almost complete bleaching because the bleaching rate ($k_1 = b + u$, in the scheme) is much faster than the recovery rate ($k_2 = u$), which corresponds to the unbinding of mantADP. Formally, $(F_i/F_0) \approx (k_2/k_1) = (u/b+u) \ll 1$ (see Appendix). Instead, the bleaching is only partial ($F_i/F_0 \approx 0.4$). This indicates that there is a site that does not bleach; we call this the nonbleaching component. Therefore, the bleaching curves indicate that there are at least three components: a slow-recovering component, a nonbleaching component, and a nonrecovering component.

The three-component model provides a good fit to the experimental data (Fig. 4). In Fig. 4 *B*, the experimental data are shown in red circles; the fitted sum of the three components is shown with a solid blue curve; and the slow-recovering, nonbleaching, and nonrecovering components

TABLE 2 Measured Parameters

Parameter		Mean ± Standard Error
Timescales		
Bleaching rate	k_1	0.70 ± 0.06 s^{-1}
Recovery rate	k_2	0.027 ± 0.004 s^{-1}
Relative fluorescence intensities		
Initial	F_0	0.068 ± 0.008
Intermediate	F_i	0.027 ± 0.003
Recovery	F_r	0.045 ± 0.003

Parameters were measured from the bleaching and recovery curves like those shown in Fig. 2 for 10 separate experiments at 1 μM mantATP, with 50–150 axonemes analyzed in each experiment. The value of the intermediate level obtained by fitting the bleaching curves was similar to the value obtained by fitting the recovery curves (bleaching: 0.027 ± 0.003, recovery: 0.027 ± 0.003; mean ± Standard Error, $n = 10$ experiments).

$$\begin{array}{ccccccc} & & k_+ & & h & & u \\ \mathrm{M} + \mathrm{T}^* & \rightleftarrows & \mathrm{MT}^* & \rightarrow & \mathrm{MD}^* & \rightarrow & \mathrm{M} + \mathrm{D}^* \\ & & k_- & & & & \\ & & b\downarrow & & \downarrow b & & \\ & & & & h & & u \\ \mathrm{M} + \mathrm{T} & \leftarrow & \mathrm{MT} & & \rightarrow \mathrm{MD} & \rightarrow & \mathrm{M} + \mathrm{D} \\ & & k_- & & & & \end{array}$$

FIGURE 3 General scheme for mantATP binding, hydrolysis, and bleaching. Fluorescent mantATP*, denoted by T*, binds rapidly and reversibly to a site M. MantATP* is hydrolyzed and phosphate released to produce mantADP*, denoted by D*, and both the unbleached mantADP*and the bleached mantADP†, denoted by D, unbind slowly with rate u, limiting the recovery rate.

are shown with a dotted light blue, dot-dashed green, and dashed black curves, respectively. The bleaching rate, the unbinding rate, and amplitudes of the three components are given in Table 3. All three components have similar amplitudes. Because the bleaching phase did not resolve into two exponentials, the bleaching rates for the nonrecovering and slow components must be similar.

Reducing dynein in axonemes using mutants and salt extraction

To determine whether axonemal dynein is contributing to one of the three binding sites, we used axonemes with different dynein contents. One way to reduce the number of dyneins is to use mutants lacking some of the dynein arms. Another way is use axonemes whose dyneins have been extracted with KCl (14). We compared wild-type axonemes, *oda1* mutant axonemes (which are missing outer dynein arms), and salt-extracted *oda1* axonemes to further reduce the number of dyneins. The amount of dynein in each type of axoneme was measured by scanning SDS-PAGE gels. *Oda1* axonemes have less dynein than wild-type axonemes. Increasing the KCl salt concentration in

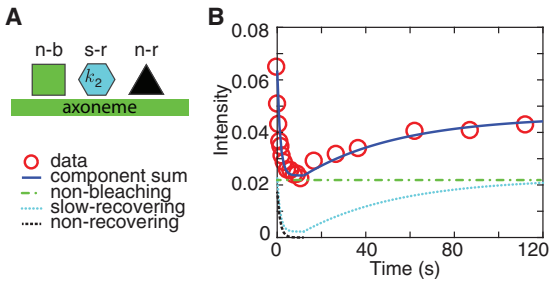

FIGURE 4 Three-component model. (*A*) The three-binding-site model with distinct kinetic characteristics is shown. See text for details. (*B*) An overlay of the three-component model and experimental data is shown. Experimental data are shown with red circles, nonrecovering component with a dashed black curve, nonbleaching (fixed) component with a dash-dotted green curve, and slow-recovering component with a dotted light blue curve. Sum of components is shown with a solid dark blue curve. To see this figure in color, go online.

TABLE 3 Molecular Rate Constants and Amplitudes of the Three Components

Parameter		Mean ± Standard Error
Timescales		
Bleaching rate constant	b	0.57 ± 0.12 s^{-1}
Unbinding rate constant	u	0.023 ± 0.003 s^{-1}
Relative amplitudes of components		
Nonrecovering	F_x	0.32 ± 0.03
Nonbleaching	F_f	0.40 ± 0.02
Slow-recovering	F_s	0.28 ± 0.02

The parameters from Table 2 were used to infer the properties of the three components. The nonrecovering component has relative amplitude $(F_0 - F_r)/F_0$. The slow-recovering component has amplitude $[(F_r - F_i)/F_0][k_1/(k_1 - k_2)] \approx (F_r - F_i)/F_0$. The nonbleaching component is the rest and is approximately equal to F_i/F_0.

oda1 axonemes further decreased the amount of dynein in the axonemes (Fig. 5 *A*). Thus, by extracting the *oda1* axonemes using salt, the dynein content could be decreased by as much as 75% compared to wild type.

Dynein reduction reduces the amplitude of the slow component

To find out whether dynein is responsible for the slow or fixed components, we compared axonemes with different amounts of dynein. In Fig. 5 *B*, an *oda1* axoneme (inner-arm dynein only) without salt extraction is compared to an *oda1* axoneme extracted with 1 M KCl. The steady-state bleaching intensity F_i was similar for both kinds of axonemes, whereas the recovery amplitude decreased significantly for the extracted axoneme, suggesting that dynein makes a contribution to the nonbleaching component but not the slow-recovering component.

These findings were confirmed in several experiments. There was no decrease, on average, in the nonbleaching component (steady-state bleaching intensity F_i) due to loss of outer-arm dynein or addition of salt to *oda1* axonemes (Fig. 6 *A*, $t(24) = 1.61$, $p > 0.12$). By contrast, the slow-recovering component decreased by more than 80% with salt concentration, and the decrease was statistically significant (Fig. 6 *B*, $slope = -0.013$, $t(24) = 5.85$, $p < 0.001$). Thus, although the nonbleaching component is not dynein, the slow-recovering component is likely to be axonemal dynein. It is possible that outer-arm dynein also makes a contribution to the slow-recovering component because the slow-recovering component is larger in the wild type versus *oda1* mutants (Fig. 6 *B*). However, the increase was not significant ($t(8.8) = 1.03$, $p > 0.32$) because of the variability in both dynein content and mantATP binding in wild-type axonemes. It is possible that our wild-type axonemes lost outer arms during preparation.

In summary, it is likely that mantATP binds to inner-arm dyneins, consistent with earlier findings (see Introduction).

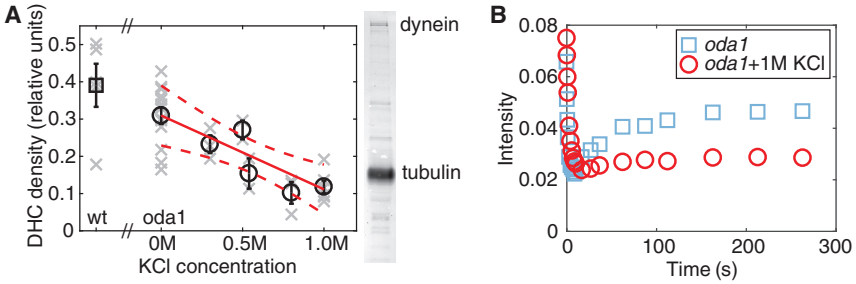

FIGURE 5 Salt extraction of dynein from the axoneme. (*A*) Salt extraction of dynein from *oda1* axonemes was performed with various concentrations of KCl. Black markers represent the mean and standard error; in light gray, data from single experiments are shown, the solid red line is a weighted linear regression of the data ($y = 0.31–0.20x$, slope significant $t(4) = -4.7$, $p < 0.01$), and dashed red curves show 95% confidence bounds. Wild-type axoneme density is represented by a square marker; the abscissa is selected arbitrarily. On the right is an example of an SDS-PAGE gel lane, showing the dynein and tubulin bands of *oda1* axoneme. (*B*) An example of measurements for *oda1* axonemes (*blue squares*) and *oda1* axonemes extracted with 1 M KCl (*red circles*) is shown. A decrease in the amplitude of the recovery (slow component $F_r - F_i$) can be seen, whereas the nonrecovering component (F_i) remains unchanged. To see this figure in color, go online.

It is also possible that mantATP binds to outer-arm dynein; however, the large variability of the rate for wild-type axonemes precluded us from making a definitive statement one way or the other. By contrast, the nonbleaching component is not dynein because its amplitude was not diminished in salt-extracted *oda1* axonemes. The nonrecovering component, which irreversibly bleaches during the experiment, is also not dynein because it was still present in the salt-extracted *oda1* axonemes. Thus, only the slow-recovering component is likely to be dynein.

The bleaching and recovery rates, as well as the amplitudes of the three components, showed little dependence on mantATP concentration

To test whether the slow component is limited by the availability of mantATP, we varied the concentration of mantATP in the assay. Imaging conditions allowed us to vary the fluorescent nucleotide concentration only over a range of 0.1–30 μM. At the lowest concentration, the axonemes were so faint as to be barely visible against the background; at the highest concentration, the background was so bright that the axoneme could be barely discerned.

The recovery rate constant showed little dependence on the mantATP concentration (Fig. 6 *C*). This is expected because the unbinding of the bleached mantATP is not expected to be influenced by the mantATP in solution (Eq. 12). The bleaching rate was also little affected by mantATP (Fig. 6 *D*). For the nonrecovering site, this is consistent with its very slow release of bleached mantATP (>100 s). For the slow-recovering site, the lack of dependence on mantATP implies that even at 0.1 μM, most of the binding sites must be occupied (Eq. 10), implying a high affinity $K_D = k_+/k_- \leq 0.1$ μM. These data suggest that both the nonrecovering and slow-recovering sites are high affinity, consistent with the relative amplitudes of the respective components showing little dependence on mantATP concentration (Fig. 6, *G* and *H*). The relative amplitude of the nonbleaching component increases somewhat with mantATP (Fig. 6 *F*), as does its absolute amplitude; this might indicate that there is a low-affinity nonbleaching component. In summary, the bleaching and recovery curves show little dependence on the mantATP concentration.

DISCUSSION

Using UV-TIRF, we visualized mantATP binding to the axoneme and found nucleotide-binding sites distributed approximately uniformly along the axoneme. The bleaching and recovery experiments indicate that there are at least three components: nonrecovering, nonbleaching, and slow-recovering.

We suggest the following interpretations of these components, which have approximately equal amplitudes.

1) The slow-recovering component is a mantATP binding site on axonemal dynein that hydrolyzes mantATP and releases the product mantADP only slowly, with rate $u = 0.023$ s^{-1}. The bleaching rate and the amplitude of this component depend only weakly on the mantATP concentration, indicating that the rate of binding of mantATP is much greater than the bleaching rate at all mantATP concentrations.
2) The nonrecovering component could correspond to a high-affinity binding site that unbinds mantATP or mantADP very slowly (on the timescale of the experiment; $\tau_u > 300$ s) so that once bleached, there is no measurable recovery. This explains the absence of a dependence of the bleaching rate and the amplitude of this component on the mantATP concentration.
3) The nonbleaching component has two interpretations. It could correspond to a very long-lasting fluorescent state of mantATP or mantADP in the axoneme microenvironment that is resistant to bleaching ($\tau_b > 300$ s). Alternatively, this component could correspond to a rapidly exchanging, nonhydrolyzing site with fast unbinding and binding rates compared to the sampling rate of 0.1 s.

If the slow-recovering component corresponds to axonemal dynein and the slow recovery is due to the unbinding of mantADP, this could account for the slow beating of *Chlamydomonas* axonemes in mantATP, as previously

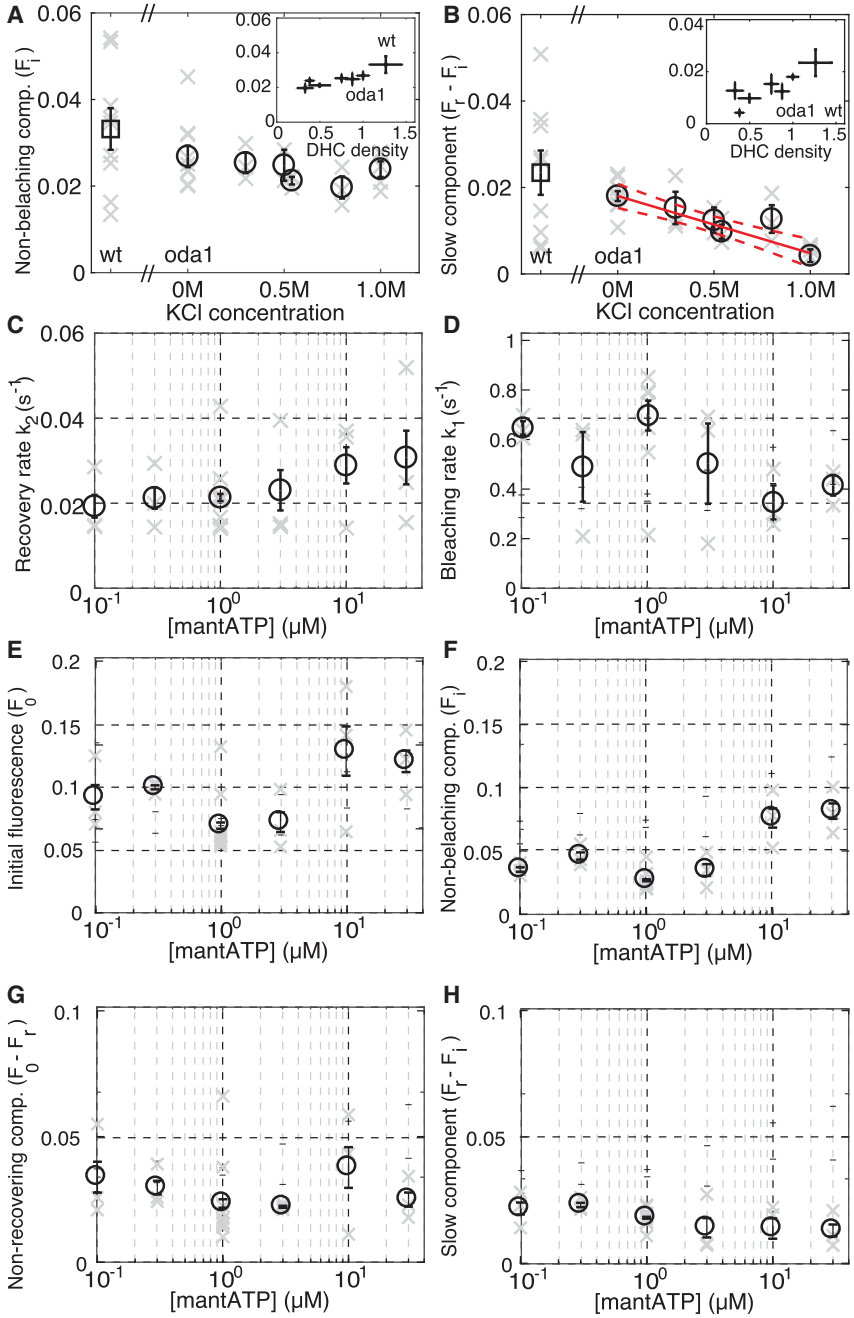

FIGURE 6 Dependencies of the fast and slow components on dynein content and mantATP concentration. (*A*) The nonbleaching component amplitude, F_i, at 1 μM mantATP is shown. Inset shows the same data, plotted against measured density of the dynein heavy chain (using Fig. 4). (*B*) Corresponding plot for the slow component amplitude, $F_r - F_i$, at 1 μM mantATP is shown. Data are plotted as mean $\pm$ standard error (*left* to *right*: $n = 9, 10, 3, 2, 3, 3, 5$). A linear regression through the salt data is shown with a solid red line (*slope* $= -0.013$; $t(24) = 5.85$; $p < 0.001$); dashed curves indicate 95% confidence bounds. Inset shows the same data, plotted against measured density of the dynein heavy chain. For both (*A*) and (*B*), data are plotted as mean $\pm$ standard error (*left* to *right*: $n = 9, 10, 3, 2, 3, 3, 5$). The mean and standard error for wild-type axonemes are indicated with a square marker to the left of the *x* axis break. Amplitudes for the salt-extracted axonemes are plotted against the salt concentration to the left of the *x* axis break. (*C*) Plot of recovery rate constant k_2 against mantATP concentration on a semilogarithmic scale is shown. (*D*) Plot of bleaching constant k_1 against mantATP concentration on a semilogarithmic scale is shown. (*F*) Intensity of nonbleaching component F_i plotted against mantATP concentration is shown. (*G*) Intensity of nonrecovering component $F_0 - F_r$ plotted against mantATP concentration is shown. (*H*) Relative intensity of slow component $F_r - F_i$ plotted against mantATP concentration is shown. For (*C*)–(*H*), data are shown as mean $\pm$ standard error ($n = 3, 3, 10, 3, 3, 3$). To see this figure in color, go online.

proposed (21). The hydrophobic methylanthraniloyl substituent on the ribose may make the affinity for the analog to the hydrophobic dynein binding pocket higher, reducing the off rate. We found that isolated demembranated *oda1* axonemes do not beat at mantATP concentrations at or below 60 μM (24). At 100 μM mantATP, they reactivate and have a beat frequency of 0.4 Hz (24). Note that the mantATP requirement for *Chlamydomonas* is much higher than previously reported for sea-urchin sperm, which has a beat frequency of 0.3 Hz at 2.5 μM mantATP (23). Unfortunately, we could not study the binding and bleaching dynamics of *Chlamydomonas* axonemes at high enough concentrations to reactivate the beat because of the poor signal/noise ratios. If one mantATP is hydrolyzed per dynein per beat cycle, at 100 μM mantATP, we expect a dynein turnover rate of 0.4 s^{-1}, and this must be faster than all rate constants between different states within the cycle, including mantADP unbinding. However, the recovery rate in our measurements was $\sim$0.02 s^{-1}. If this rate corresponds to mantADP release, then release would need to be accelerated severalfold for beating at 0.4 Hz to occur. Therefore, we propose (assuming that our measured recovery rate corresponds to mantADP

release) that either beating itself accelerates mantADP release or that preventing beating through immobilization on the surface inhibits mantADP release. Thus, our observations are consistent with axonemal dyneins showing force-dependent inhibition. This is consistent with an earlier observation that dynein motors in the axoneme continue generating force even when the axoneme is prevented from beating, perhaps because of inhibition of dynein detachment by force (30).

We used a mixture of 2′- and 3′-mantATP. These isomers can have different binding characteristics (31); however, we only observed one distinct recovery rate for dynein in our assay, so we cannot distinguish between the two isoforms.

It is known that dynein has multiple nucleotide-binding sites with distinct nucleotide-binding properties, of which one is responsible for motility (26,32–34). Previous work has shown that mantATP binds to sea urchin outer-arm dynein with dissociation constants 4 and 60 μM (26). We observed binding of mantATP to the slow-recovering site (presumed to be dynein) even at 0.1 μM mantATP. The higher affinity in our experiments might be due to the dynein being in a different chemomechanical environment while it is in the intact, immobilized axoneme.

Directly observing labeled nucleotides bound to the axoneme is a promising method for characterizing dynein activity in the intact axoneme. If the fluorescence could be resolved in space and time, the traveling wave of activation of dynein could, in principle, be measured. The biggest difficulty currently is that dynein is very selective for which nucleotides it can utilize. We found that mantATP gives very low signals. Development of new fluorophores and conjugation methods is ongoing as demand grows for new and more stable fluorescent dyes. This gives us hope that a fluorescently labeled ATP suitable for dynein, with better optical characteristics, may be available in the future.

The use of TIRF microscopy assisted us in reducing the background of diffusing labeled ATP in solution by illuminating only ~200 nm from the surface of the cover glass. The method works very well for observing axonemes that are attached to the surface. Once the axoneme is beating, it will likely be too far from the surface of the glass chamber for this method. It must also be noted that the beat of the axoneme is not planar. It is more suitable to use epifluorescence microscopy for observations of fluorescence in the beating axoneme. To minimize background noise from diffusing fluorophore, a spiking assay, using a mixture of labeled and unlabeled ATP, could be used. This will require using a fluorescent dye that allows near-single-molecule dye resolution.

There are other important aspects to consider if one is to perform spatiotemporally resolved observation of dynein activity in a beating axoneme. The dynein proteins may be active all the time. In the case that the motors are at least downregulated when not producing force, there would still be a possibility of resolving the wave of force. The motors are also likely to be alternately active on different sides of the axoneme, making it harder to resolve their activity.

Careful separation of contributions from dynein and other proteins is also important, as well as being aware of the existence of regulatory sites. Further studies on mutant axonemes with various nondynein components missing might shed light on the source of the nondynein components and possible kinase or nondynein motor activity in the axoneme. We hope that with this investigation, we lay the groundwork for future successful observation of dynein in the intact beating axoneme.

APPENDIX

In this section, we solve the kinetic scheme shown in Fig. 3 under simplifying assumptions. The total concentration of binding states is

$$[\mathrm{M_{tot}}] = [\mathrm{M}] + [\mathrm{MT^*}] + [\mathrm{MT}] + [\mathrm{MD^*}] + [\mathrm{MD}],$$

where M corresponds to the nucleotide-binding protein in the apo state, T* is fluorescent mantATP, D* is fluorescent mantADP, T is bleached mantATP, and D is bleached mantADP. k_+ is the second-order rate constant for mantATP binding to M, and k_- is the unbinding rate. For *Tetrahymena* outer-arm dynein, Holzbaur and Johnson (29) found $k_{+,\mathrm{ATP}} = 4\ \mu\mathrm{M}^{-1}\ \mathrm{s}^{-1}$ and $k_{-,\mathrm{ATP}} = 0.15\ \mathrm{s}^{-1}$ for ATP binding and unbinding, respectively. We assume that [T*] is constant because the TIRF illumination depth (~0.2 μm) is only a small fraction of the 100-μm depth of the flow cell, and so bleaching of the mantATP in solution will be ≈500 times slower than that in the TIRF field. As a shorthand, we write $k = k_+[\mathrm{T^*}]$, which is 4 s^{-1} at 1 μM ATP. The rate constant h combines hydrolysis and phosphate ($\mathrm{P_i}$) release and is irreversible because the phosphate concentration in solution is negligible. For the axonemal dynein ATPase, hydrolysis is fast and reversible (rates of 100 and 30 s^{-1}, respectively), and phosphate release is also fast (80 s^{-1}) (29): we therefore denote MT* and MT as combined ATP and ADP • $\mathrm{P_i}$ states with $(100/(100+30+80))80$. u is the unbinding rate of the mantADP (D* and D), assumed not to depend on whether mantADP is bleached or not; the reverse rate is zero because the concentrations of D* and D in solution are negligible. $u_{\mathrm{ADP}} \approx 4\ \mathrm{s}^{-1}$ is the rate-limiting step for the dynein ATPase and is increased up to fivefold in the presence of microtubules (29). b is the bleaching rate, which is irreversible.

We now make the simplifying assumption that $h \gg k_-, b, u$. This assumption is true for ATP (given that the bleaching rate is $b \approx 0.6\ \mathrm{s}^{-1}$, Table 3), and will be true for mantATP provided that hydrolysis is not disproportionally decreased. With this assumption, the kinetic scheme reduces to

$$\begin{array}{ccccc} & \overset{k}{} & & \overset{u}{} & \\ \mathrm{M} + \mathrm{T^*} & \rightarrow & \mathrm{MD^*} & \rightarrow & \mathrm{M} + \mathrm{D} \\ & & \downarrow b & & \\ & & & \overset{u}{} & \\ & & \mathrm{MD} & \rightarrow & \mathrm{M} + \mathrm{D} \end{array}$$

This has a simple solution. The steady-state fluorescence in the absence of bleaching is

$$F_0 = \frac{[\mathrm{MD^*}]}{[\mathrm{M_{tot}}]} = \frac{k}{k+u}$$

and in the presence of bleaching

$$F_i = \frac{u}{b+u}\ \frac{k}{k+u} \approx \frac{u}{b+u} F_0$$

There are two rate constants, $k + u$ and $b + u$: taking k large, we obtain the rate constants $k_1 = b + u$ in the presence of bleaching and $k_2 = u$ in the absence of bleaching (i.e., during recovery). Thus,

$$F_i \approx \frac{k_2}{k_1} F_0,$$

as stated in the main text after Fig. 3.

AUTHOR CONTRIBUTIONS

M.F. and J.H. designed the experiments. M.F. preformed the experiments and image and data analysis. J.H. and M.F. constructed the model. M.M. designed and M.M. and M.F. built the microscope setup. M.F. and J.H. wrote the manuscript in consultation with M.M.

ACKNOWLEDGMENTS

The authors thank the anonymous reviewers as well as the editor for their insightful suggestions, Dr. Mark Kittisopikul for useful suggestions about the image analysis, and Dr. Veikko Geyer for discussions and advice throughout the course of this work.

REFERENCES

1. Carvalho-Santos, Z., J. Azimzadeh, …, M. Bettencourt-Dias. 2011. Evolution: tracing the origins of centrioles, cilia, and flagella. *J. Cell Biol.* 194:165–175.
2. Nicastro, D., C. Schwartz, …, J. R. McIntosh. 2006. The molecular architecture of axonemes revealed by cryoelectron tomography. *Science.* 313:944–948.
3. Li, J. B., J. M. Gerdes, …, S. K. Dutcher. 2004. Comparative genomics identifies a flagellar and basal body proteome that includes the BBS5 human disease gene. *Cell.* 117:541–552.
4. Gibbons, I. R., and A. J. Rowe. 1965. Dynein: a protein with adenosine triphosphatase activity from cilia. *Science.* 149:424–426.
5. Summers, K. E., and I. R. Gibbons. 1971. Adenosine triphosphate-induced sliding of tubules in trypsin-treated flagella of sea-urchin sperm. *Proc. Natl. Acad. Sci. USA.* 68:3092–3096.
6. Johnson, K. A. 1985. Pathway of the microtubule-dynein ATPase and the structure of dynein: a comparison with actomyosin. *Annu. Rev. Biophys. Biophys. Chem.* 14:161–188.
7. Chen, D. T. N., M. Heymann, …, Z. Dogic. 2015. ATP consumption of eukaryotic flagella measured at a single-cell level. *Biophys. J.* 109:2562–2573.
8. Brokaw, C. J. 1991. Microtubule sliding in swimming sperm flagella: direct and indirect measurements on sea urchin and tunicate spermatozoa. *J. Cell Biol.* 114:1201–1215.
9. Johnson, K. A., S. P. Marchese-Ragona, …, T. J. Chilcote. 1986. Dynein structure and function. *J. Cell Sci. Suppl.* 5:189–196.
10. Ueno, H., K. H. Bui, …, T. Ishikawa. 2014. Structure of dimeric axonemal dynein in cilia suggests an alternative mechanism of force generation. *Cytoskeleton (Hoboken).* 71:412–422.
11. Sakakibara, H., and K. Oiwa. 2011. Molecular organization and force-generating mechanism of dynein. *FEBS J.* 278:2964–2979.
12. Lin, J., and D. Nicastro. 2018. Asymmetric distribution and spatial switching of dynein activity generates ciliary motility. *Science.* 360:eaar1968.
13. Yokota, E., and I. Mabuchi. 1994. C/A dynein isolated from sea urchin sperm flagellar axonemes. Enzymatic properties and interaction with microtubules. *J. Cell Sci.* 107:353–361.
14. Bui, K. H., T. Yagi, …, T. Ishikawa. 2012. Polarity and asymmetry in the arrangement of dynein and related structures in the Chlamydomonas axoneme. *J. Cell Biol.* 198:913–925.
15. Machin, K. E. 1958. Wave propagation along flagella. *J. Exp. Biol.* 35:796–806.
16. Sartori, P., V. F. Geyer, …, J. Howard. 2016. Dynamic curvature regulation accounts for the symmetric and asymmetric beats of Chlamydomonas flagella. *ELife.* 5:e13258.
17. Lindemann, C. B. 1994. A model of flagellar and ciliary functioning which uses the forces transverse to the axoneme as the regulator of dynein activation. *Cell Motil. Cytoskeleton.* 29:141–154.
18. Brokaw, C. J. 1975. Molecular mechanism for oscillation in flagella and muscle. *Proc. Natl. Acad. Sci. USA.* 72:3102–3106.
19. Riedel-Kruse, I. H., A. Hilfinger, …, F. Jülicher. 2007. How molecular motors shape the flagellar beat. *HFSP J.* 1:192–208.
20. Inoue, Y., and C. Shingyoji. 2007. The roles of noncatalytic ATP binding and ADP binding in the regulation of dynein motile activity in flagella. *Cell Motil. Cytoskeleton.* 64:690–704.
21. Lark, E., and C. K. Omoto. 1994. Axonemes paralyzed by the presence of dyneins unable to use ribose-modified ATP. *Cell Motil. Cytoskeleton.* 27:161–168.
22. Shimizu, T., K. Furusawa, …, R. D. Vale. 1991. Nucleotide specificity of the enzymatic and motile activities of dynein, kinesin, and heavy meromyosin. *J. Cell Biol.* 112:1189–1197.
23. Omoto, C. K. 1992. Sea urchin axonemal motion supported by fluorescent, ribose-modified analogues of ATP. *J. Muscle Res. Cell Motil.* 13:635–639.
24. Feofilova, M. 2016. Probing dynein motor activity in the intact chlamydomonas axoneme. PhD thesis. Technische Universität Dresden.
25. Kikushima, K. 2009. Central pair apparatus enhances outer-arm dynein activities through regulation of inner-arm dyneins. *Cell Motil. Cytoskeleton.* 66:272–280.
26. Mocz, G., M. K. Helms, …, I. R. Gibbons. 1998. Probing the nucleotide binding sites of axonemal dynein with the fluorescent nucleotide analogue 2′(3′)-O-(-N-Methylanthraniloyl)-adenosine 5′-triphosphate. *Biochemistry.* 37:9862–9869.
27. Alper, J. D., M. Tovar, and J. Howard. 2013. Displacement-weighted velocity analysis of gliding assays reveals that Chlamydomonas axonemal dynein preferentially moves conspecific microtubules. *Biophys. J.* 104:1989–1998.
28. Alper, J., V. Geyer, …, J. Howard. 2013. Reconstitution of flagellar sliding. *Methods Enzymol.* 524:343–369.
29. Holzbaur, E. L., and K. A. Johnson. 1989. Microtubules accelerate ADP release by dynein. *Biochemistry.* 28:7010–7016.
30. Schmitz, K. A., D. L. Holcomb-Wygle, …, C. B. Lindemann. 2000. Measurement of the force produced by an intact bull sperm flagellum in isometric arrest and estimation of the dynein stall force. *Biophys. J.* 79:468–478.
31. Oiwa, K., J. F. Eccleston, …, D. R. Trentham. 2000. Comparative single-molecule and ensemble myosin enzymology: sulfoindocyanine ATP and ADP derivatives. *Biophys. J.* 78:3048–3071.
32. Gibbons, I. R., B. H. Gibbons, …, D. J. Asai. 1991. Multiple nucleotide-binding sites in the sequence of dynein beta heavy chain. *Nature.* 352:640–643.
33. Ogawa, K. 1991. Four ATP-binding sites in the midregion of the beta heavy chain of dynein. *Nature.* 352:643–645.
34. Tani, T., and S. Kamimura. 1999. Dynein-ADP as a force-generating intermediate revealed by a rapid reactivation of flagellar axoneme. *Biophys. J.* 77:1518–1527.